

GRAVITATIONAL WAVES AND X-RAY SIGNALS FROM STELLAR DISRUPTION BY A MASSIVE BLACK HOLE

SHIHO KOBAYASHI,^{1,2} PABLO LAGUNA,^{1,2} E. STERL PHINNEY,³ AND PETER MÉSZÁROS^{1,2,4}

Received 2004 April 7; accepted 2004 July 22

ABSTRACT

Gravitational waves and X-ray flares are expected from tidal disruption of stars by a massive black hole. Using a relativistic smoothed particle hydrodynamics code, we investigate the fate of main-sequence and helium stars in plunge orbits passing near Schwarzschild or Kerr black holes of mass $\sim 10^5$ – $10^6 M_\odot$. We show that quadrupole gravitational waves emitted during the tidal disruption process are described reasonably well by a point-particle approximation even in the strong-encounter case. An additional hydrodynamic calculation based on the Godunov method indicates that shocks develop for sufficiently high tidal compressions. The shock heating results in an X-ray flare, which for solar-type stars disrupted by $\sim 10^6 M_\odot$ black holes is in the keV range associated with the gravitational wave signal. The hardness and duration of the X-ray flare may serve as a diagnostic of the mass of the central black hole.

Subject headings: black hole physics — galaxies: nuclei — gravitational waves — hydrodynamics —
X-rays: bursts

1. INTRODUCTION

There is strong evidence, based on stellar kinematics and gasdynamics, for the existence of massive black holes with masses from a few times 10^5 to a few times $10^9 M_\odot$ in the center of a substantial fraction of galaxies (e.g., Kormedy & Gebhardt 2001). Gravitational radiation caused by stars orbiting closely around such black holes is one of the most promising candidates for detection by the *Laser Interferometer Space Antenna (LISA)*; e.g., Bender 1998; Hils & Bender 1995; Sigurdsson & Rees 1997; Ivanov 2002; Freitag 2003). Compact stars (white dwarfs, neutron stars, or stellar mass black holes) in bound orbits relatively close to the black hole will emit gravitational waves as they spiral all the way down to the horizon. Although the detection of such waves requires a set of accurate wave templates and significant computational power to search the large dimensionality parameter space, tracking the signals over a large number of cycles boosts the strength of the signals; hence, previous studies have mainly addressed the gravitational waves from such stars.

On the other hand, there is a larger reservoir of main-sequence stars that are affected by the gravitational field of the massive black hole already at large distances, where their gravitational wave emission is still negligible. Of these, only stars in almost radial orbits can approach the horizon, where they can emit strong gravitational waves, as well as being subject to tidal disruption. The rate of captures leading to disruption may be even larger for He stars. Since a single periastron passage near the tidal radius can disrupt the star, the detectable gravitational wave signal takes the form of a burst. However, the gravitational waves are also expected to be associated with X-ray/UV emission originating from the tidal compressional heating and disruption of the star. The detection of the photon flares provides the means for pinpointing the

direction, occurrence time, and possibly the redshift of the event, as well as for obtaining independent evidence for the existence and properties of the massive black hole. The temporal coincidence of gravitational wave and electromagnetic signals could enhance the confidence level of the detection of both signals (e.g., Finn et al. 1999). Multiwindow observations (gravitational and electromagnetic emissions) might allow us to set tighter constraints on the properties of both the massive black hole and the star.

Here we study the gravitational and electromagnetic radiation from the tidal disruption of a main-sequence star and a helium star by a massive black hole. We use a three-dimensional relativistic smoothed particle hydrodynamics (SPH) code (Laguna et al. 1993a) and investigate the gravitational wave and photon emission accompanying the tidal disruption event. In § 2 we discuss the main features of the tidal disruption process and the photon flares expected during the disruption process. In § 3 we provide a rough estimate of the characteristics of the gravitational waves. In § 4 we discuss the numerical results obtained from relativistic SPH calculations around both Schwarzschild and maximally rotating Kerr black holes. In § 5 the detectability of the gravitational waves and the constraints obtainable from photon and gravitational wave observations are discussed. Conclusions and discussions are given in § 6. In the Appendix we discuss the shock formation during the tidal compression, using a relativistic Lagrangian code based on the Godunov method (Kobayashi et al. 1999).

2. STELLAR DISRUPTION

The tidal disruption radius R_t is the distance from a black hole at which the tidal acceleration due to the black hole equals the self-gravity of the star. A simple estimate is

$$R_t \sim R_* \left(\frac{M_h}{M_*} \right)^{1/3} \sim 7 \times 10^{12} \left(\frac{R_*}{R_\odot} \right) \left(\frac{M_*}{M_\odot} \right)^{-1/3} \left(\frac{M_h}{10^6 M_\odot} \right)^{1/3} \text{ cm}, \quad (1)$$

where M_h is the mass of the black hole and M_* and R_* are the mass and radius of the star, respectively. Thus, for a solar-type star, the ratio between the tidal disruption radius R_t and the

¹ Department of Physics and Center for Gravitational Wave Physics, Pennsylvania State University, University Park, PA 16802.

² Department of Astronomy and Astrophysics, Pennsylvania State University, University Park, PA 16802.

³ California Institute of Technology, Pasadena, CA 91125.

⁴ Institute for Advanced Study, Princeton, NJ 08540.

event horizon scale $R_g = 2GM_h/c^2 \sim 3 \times 10^{11} (M_h/10^6 M_\odot) \text{ cm}$ is

$$\frac{R_t}{R_g} \sim 24 \left(\frac{R_*}{R_\odot} \right) \left(\frac{M_*}{M_\odot} \right)^{-1/3} \left(\frac{M_h}{10^6 M_\odot} \right)^{-2/3}. \quad (2)$$

When the black hole mass is small enough ($M_h \lesssim 10^8 M_\odot$ for solar-type stars), the tidal disruption radius R_t lies outside the event horizon, and the star is disrupted before falling in. In Figure 1, we plot the tidal radii and the event horizon scales for various types of stars as a function of the black hole mass. Prompt disruption occurs when stars are scattered into highly eccentric (loss cone) orbits with periastron distances $R_p < R_t$. The strength of the tidal encounter is characterized by a penetration factor β_p defined as

$$\beta_p = \frac{R_t}{R_p}. \quad (3)$$

The tidal disruption of stars by massive black holes has been investigated by many authors both analytically and numerically (e.g., Carter & Luminet 1982, 1983; Lacy et al. 1982; Nolthenius & Katz 1982; Luminet & Marck 1985; Rees 1988; Evans & Kochanek 1989; Laguna et al. 1993b; Khokhlov et al. 1993; Marck et al. 1996; Loeb & Ulmer 1997; Ulmer et al. 1998; Ayal et al. 2000; Ivanov & Novikov 2001). During the dynamical evolution of a main-sequence or a giant star, several mechanisms related to the tidal force of a massive black hole can lead to electromagnetic radiation from the star or the resulting debris. Among these, the tidal compression and the fallback of stellar debris are likely to be most important in the context of the association with gravitational radiation.

Tidal compression.—For a star penetrating well inside the tidal radius, $\beta_p > 1$, the tidal disruption will be preceded by a short-lived phase of high compression of the star. In the extreme case of $\beta_p \gg 1$, the strong compression has been conjectured to cause a supernova-like thermonuclear detonation event (Carter & Luminet 1982). However, even in the absence of a detonation, the thermal energy produced by the compression may lead to X-ray emission around the compression point, as we discuss below.

A star penetrating deeply within the tidal radius of a massive black hole undergoes significant compression. Each section of the star is squeezed through a point of maximum compression at a fixed point on the star's orbit (see Fig. 4 in Luminet & Marck 1985). This occurs on a timescale comparable to the crossing time of the star through the compression point,

$$\delta t \sim \frac{R_*}{v_p} \sim 10 \left(\frac{M_*}{M_\odot} \right)^{-1/6} \left(\frac{R_*}{R_\odot} \right)^{3/2} \left(\frac{M_h}{10^6 M_\odot} \right)^{-1/3} \text{ s}, \quad (4)$$

where $v_p \sim c(R_g/R_t)^{1/2}$ is the orbital velocity at periastron. The distortions $\Delta R_*/R_* \sim 1$ imply bulk flow velocities of order $R_*/\delta t \sim 10^{10} \text{ cm s}^{-1}$. Adiabatic compression alone can only increase the stellar surface and interior layer temperatures by a factor $\lesssim 10$, implying a sound speed $c_s \sim (GM_*/R_*)^{1/2} \sim 10^8 \text{ cm s}^{-1}$. If this were the only heating, the adiabatic response time of the flow to the varying potential would be $\sim R_*/c_s \sim 10^3 \text{ s}$, which is much longer than the dynamic crossing time (eq. [4]). This implies a very large Mach number and strongly suggests that shocks must occur. Because of the

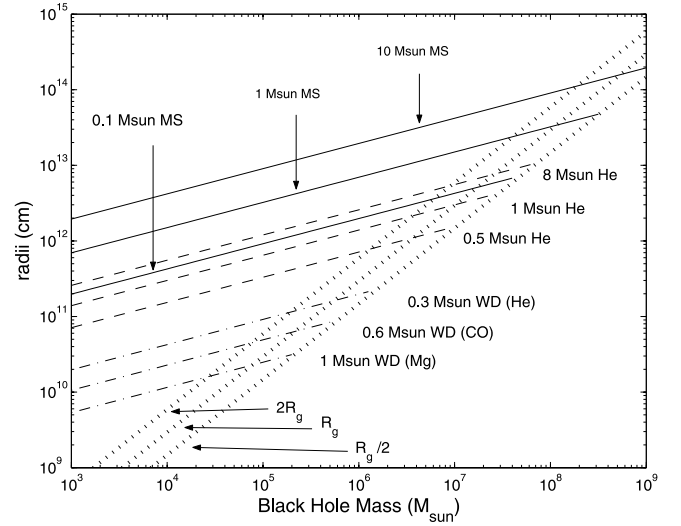


FIG. 1.—Tidal radius and event horizon scales for different stars as a function of the black hole mass, with notation $R_t = 2GM/c^2$: main-sequence stars (MS), He stars (He), and white dwarfs (WD).

complicated geometry and the large dynamic range, previous numerical experiments have not shown the development of shocks. Most calculations, however, are based on SPH methods, which are not well suited for studying shocks, but are resorted to in order to handle the complex geometry and potentials. Our SPH calculations verify the magnitude of the large distortions mentioned above, on a timescale comparable to equation (4), and we are led to conclude that shocks are likely to occur. To verify the existence of shocks, we have performed additional numerical calculations on a one-dimensional model, using a different code specifically developed for handling relativistic shocks, a Lagrangian hydrodynamic code based on the Godunov method. The numerical results, discussed in the Appendix, indicate that in deep-penetration cases $\beta_p \gg 1$ a shock does indeed develop near the periastron and propagates through the star. Shocks are the only way to rapidly heat the gas, including the surface, to temperatures of order the virial value ($\sim \text{keV}$), which are also approximately the temperatures indicated by our SPH calculations. Here we proceed on the assumption, substantiated by the above Lagrangian shock-capturing calculations, that shocks have occurred, and that the temperatures provided by the SPH calculations are approximately representative of the values resulting from the sudden shock heating occurring throughout the volume of the star.

The thermal energy E_{th} produced by the shock heating can be roughly estimated as

$$E_{\text{th}} = \frac{GM_*^2}{R_*} \sim 4 \times 10^{48} \left(\frac{M_*}{M_\odot} \right)^2 \left(\frac{R_*}{R_\odot} \right)^{-1} \text{ ergs}. \quad (5)$$

The typical temperature of the shocked star is

$$k_B T \sim \frac{GM_* m_p}{R_*} \sim 1 \left(\frac{M_*}{M_\odot} \right) \left(\frac{R_*}{R_\odot} \right)^{-1} \text{ keV}, \quad (6)$$

where m_p is the proton mass. The timescale δt (eq. [4]) gives a rough estimate for the heating time, while the cooling time from the surface layer is shorter. Hence the X-ray flare has a duration lasting approximately the crossing time (eq. [4]). Since the Thomson optical depth of the star is very large,

$\tau_T \sim M_* \sigma_T / 4\pi m_p R_*^2 \sim 10^{10} (M_*/M_\odot)(R_*/R_\odot)^{-2}$, most of the thermal energy remains trapped inside the star. However, a fraction of the thermal energy near the surface can be radiated promptly. The thermal energy in the outermost Thomson mean free path is at least $E_{\text{rad, min}} \sim (E_{\text{th}}/\tau_T) \sim 4 \times 10^{38} (M_*/M_\odot)(R_*/R_\odot)$ ergs, and an approximate lower bound on the X-ray flare luminosity is $L_{X, \text{min}} \gtrsim 4 \times 10^{37} (M_*/M_\odot)^{7/6} (R_*/R_\odot)^{-1/2} (M_h/10^6 M_\odot)^{1/3}$ ergs s^{-1} , of the order of the stellar Eddington luminosity. However, the total energy radiated during the flare (the X-ray fluence) can be larger than this, since shock heating of the surface continues over the crossing time (eq. [4]). The energy radiated from the surface during this time (eq. [4]) can be replenished by energy diffusing up from deeper layers down to a depth $D \sim (c\delta t R_*/\tau_T)^{1/2}$, which is within a diffusion time comparable to the crossing time δt . An upper limit to the thermal energy or fluence that diffuses out from this depth is

$$E_{\text{rad, peak}} \lesssim E_{\text{th}} \left(\frac{c\delta t}{R_* \tau_T} \right)^{1/2} \sim 10^{43} \left(\frac{M_*}{M_\odot} \right)^{17/12} \left(\frac{R_*}{R_\odot} \right)^{1/4} \left(\frac{M_h}{10^6 M_\odot} \right)^{-1/6} \text{ ergs.} \quad (7)$$

The corresponding upper limit on the flare luminosity is

$$L_{X, \text{peak}} \lesssim 10^{42} \left(\frac{M_*}{M_\odot} \right)^{19/12} \left(\frac{R_*}{R_\odot} \right)^{-5/4} \left(\frac{M_h}{10^6 M_\odot} \right)^{1/6} \text{ ergs s}^{-1}. \quad (8)$$

After the peak, whose duration is approximately given by equation (4), the X-ray luminosity decays as $L \sim (ct/\tau R_*)^{1/2} (E_{\text{th}}/t) \propto t^{-1/2}$. Since the crossing time δt is much shorter than the preshock expansion time of the star, $\sim R_*/c_s \sim 2 \times 10^3 (M_*/M_\odot)^{-1/2} (R_*/R_\odot)^{3/2}$ s, and at most comparable to the postshock expansion time while the emission region is thin, $D \ll R_*$, we approximate the emission region as a roughly static gas slab to obtain equations (7) and (8) and the initial decay scaling $L \propto t^{-1/2}$. A caveat concerning the prompt emission is that if a large amount of gas gets ripped off before the shock compression of the bulk of the star, the optical depth of patches of the ripped-off gas could be large enough to intercept the photons radiated along some directions, while allowing escape along others. This effect should be accounted for in the future.

Matter fallback.—After the disruption, a fraction (25% ~ 50%) of the material in the disrupted star remains gravitationally bound to the black hole (Rees 1988; Ayal et al. 2000). It returns to the periastron, giving a fallback accretion luminosity evolving with time as $\sim t^{-5/3}$ (Rees 1988; Phinney 1989). The total energy radiated during the fallback phase can be less than that in the subsequent accretion disk phase. Nevertheless, since the fallback phase is relatively short-lived ($\sim \text{yr}$), it dominates the early luminosity of a disruption event (after the prompt flare). The time since disruption for this to happen and the peak luminosity are given by (e.g., Li et al. 2002)

$$\Delta t_{\text{fallback}} \sim 10 \left(\frac{M_h}{10^6 M_\odot} \right) \left(\frac{M_*}{M_\odot} \right)^{-1} \left(\frac{R_*}{R_\odot} \right)^{3/2} \text{ days,} \quad (9)$$

$$L_{\text{fallback, peak}} \sim 10^{45} \left(\frac{f}{0.1} \right) \left(\frac{M_h}{10^6 M_\odot} \right)^{1/6} \times \left(\frac{M_*}{M_\odot} \right)^{7/3} \left(\frac{R_*}{R_\odot} \right)^{-5/2} \text{ ergs s}^{-1}, \quad (10)$$

where f is the fraction of the stellar material falling back to periastron.

Disk accretion.—The fallback material eventually settles into a disk, which is accreted on a timescale of the order of the viscous time $t_{\text{visc}} \sim 10^3$ yr (Li et al. 2002). In the present paper, we focus mainly on the prompt flash by the first of these three components.

3. GRAVITATIONAL WAVES

A main-sequence star that penetrates the tidal radius will be disrupted around the periastron, and the particles in the disrupted star follow approximately independent Keplerian orbits. The resulting stretched-out debris trail is not compact enough to emit strong gravitational waves after leaving the first closest approach. The detectable gravitational wave signal will thus have a burstlike behavior, roughly characterized by an amplitude h , a frequency f , and a duration $\tau \sim 1/f$, where

$$h \sim \frac{GM_* R_g}{c^2 D R_p} \sim 2 \times 10^{-22} \beta_p \left(\frac{D}{10 \text{ Mpc}} \right)^{-1} \left(\frac{R_*}{R_\odot} \right)^{-1} \left(\frac{M_*}{M_\odot} \right)^{4/3} \left(\frac{M_h}{10^6 M_\odot} \right)^{2/3}, \quad (11)$$

$$f \sim \left(\frac{GM_h}{R_p^3} \right)^{1/2} \sim 6 \times 10^{-4} \beta_p^{3/2} \left(\frac{M_*}{M_\odot} \right)^{1/2} \left(\frac{R_*}{R_\odot} \right)^{-3/2} \text{ Hz.} \quad (12)$$

LISA will be able to detect gravitational waves of amplitude $h \gtrsim 10^{-21}$ for burst sources in the frequency range $f \sim 10^{-4}$ to 10^{-1} Hz (Bender 1998; Hughes 2002). Gravitational waves from stellar disruption could thus be detectable if $\beta_p \gtrsim 1$ and the distance $D \lesssim 10$ Mpc. In § 4 we compare these estimates of the gravitational radiation and photon emission against more detailed results obtained with a numerical SPH code.

The disruption process can affect the amplitude and waveform of the gravitational waves. For comparison with the SPH results, it is useful to estimate the radiation from a point particle with the same mass as the star. Since highly eccentric elliptic orbits are observationally indistinguishable from an appropriate parabolic orbit, we will consider parabolic orbits for the SPH simulations and point-particle calculations. The parabolic orbit for a point particle of mass M_* around a Kerr black hole of mass M_h and spin a ($|a| < R_g/2$) is described by the following equations in the Kerr-Schild coordinates (e.g., Landau & Lifshitz 1975; Campanelli et al. 2001):

$$\left(\frac{d\varphi}{dt} - \frac{a}{\Delta} \frac{dR}{dt} \right) \left(1 - \frac{R_g R}{c\Delta} \frac{dR}{dt} \right)^{-1} = c\delta^{-1} \left[L - (L - a) \frac{R_g}{R} \right], \quad (13)$$

$$\left(\frac{dR}{dt} \right)^2 \left(1 - \frac{R_g R}{c\Delta} \frac{dR}{dt} \right)^{-2} = c^2 \left(\frac{\Delta}{\delta} \right)^2 \frac{R_g}{R} \left(1 - \frac{R_p}{R} \right) \left(1 - \frac{R_0}{R} \right), \quad (14)$$

where the orbit is assumed to be in the equatorial plane, $\delta = R^2 + a^2 - a(L - a)(R_g/R)$, $\Delta = R^2 - R_g R + a^2$, cL is the angular momentum per unit mass, and the radii R_p (periastron):

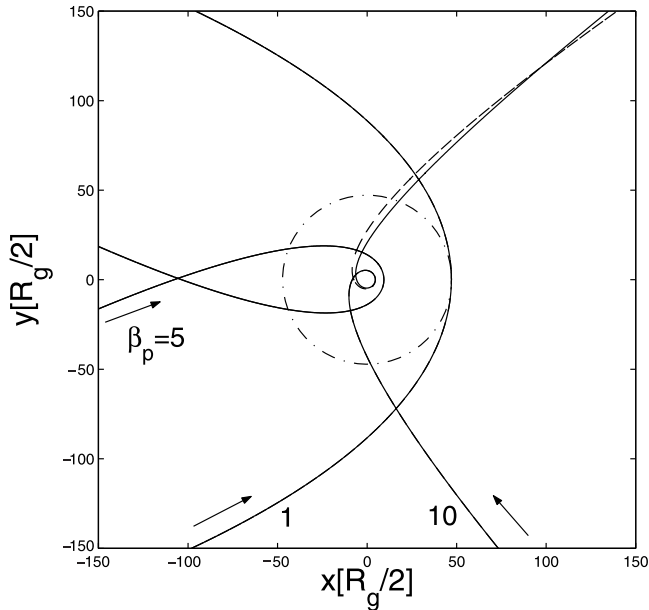


FIG. 2.—Orbits of a solar-type star with $\beta_p = 1, 5,$ or 10 around a Schwarzschild black hole: the orbit of the star's CM (solid line), compared with the point-particle orbits (dashed line). The dashed-dotted circle gives the tidal radius. The arrows indicate the motion of the stars; $M_h = 10^6 M_\odot$ and $a = 0$. The values of x - and y -coordinates are in units of $R_g/2$.

$R_p \geq R_0$) and R_0 are solutions of $R^2 - (L^2/R_g)R + (L - a)^2 = 0$. If the black hole is not rotating ($a = 0$), the smallest distance to which the test particle on a parabolic orbit can approach and yet not be captured by the black hole is $R_p \sim 2R_g$. If the black hole is maximally rotating, the closest approach possible in the equatorial plane is $R_p \sim R_g/2$ for a prograde case and $R_p \sim 2.9R_g$ for a retrograde case. For $a = 0$, the angular momentum is given by $L^2 = R_g R_p (1 - R_g/R_p)^{-1}$. Since we can express the angular momentum in terms of an impact parameter b and an asymptotic orbital velocity $v_\infty (\ll c)$ as $L = b(v_\infty/c)$, the effective cross section subtended by the black hole for penetration by the star to within a distance R_p is given by $\sigma_p = \pi b^2 = \pi (v_\infty/c)^{-2} R_g R_p (1 - R_g/R_p)^{-1}$. This has the noteworthy property of depending only linearly on $R_p (> 2R_g)$ (Carter & Luminet 1983), multiplied by a factor $R_g (c/v_\infty)^2 \gg R_p$, in contrast to the purely geometric cross section, which would be proportional to R_p^2 . The fraction of stars penetrating within the distance R_p is directly proportional to σ_p , so the fraction of stars suffering a prompt tidal disruption can be much larger than in an estimate based on the geometric cross section.

4. NUMERICAL SIMULATIONS

We employ a three-dimensional relativistic SPH code (Laguna et al. 1993b) in which the hydrodynamics is calculated in a fixed Schwarzschild or Kerr black hole background written in the ingoing Kerr-Schild form, whose coordinates are horizon-penetrating and suitable for studying the evolution of stars orbiting closely around the horizon or even falling into it. The code has a variable smoothing length, and the time integration is performed with a second-order Runge-Kutta integrator with adaptive time steps (see Laguna et al. 1993b for details). For simplicity we use a polytropic equation of state with adiabatic index $\Gamma = 5/3$ to model the stars. The density profile is obtained by solving the Lane-Emden equa-

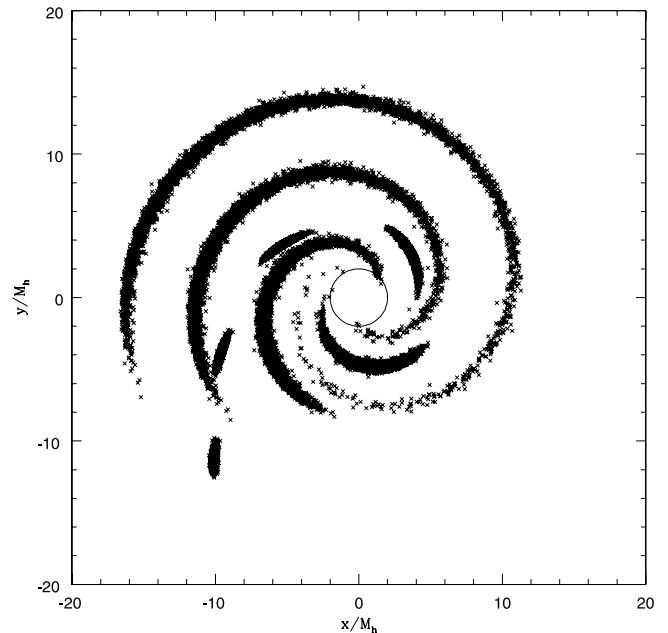


FIG. 3.—Snapshots of a disrupted star (SPH particle distribution): eight frames at $t = -335, -236, -138, -39.7, 58.6, 157, 255,$ and 353 s are superposed. The time is relative to an origin at the instant of passage through the periastron of the orbit; $\beta_p = 10, M_h = 10^6 M_\odot,$ and $a = 0$. The values of x - and y -coordinates are in units of $R_g/2 = GM_h/c^2$. The center circle shows the Schwarzschild black hole horizon $R = R_g$.

tions, and the particles (typically 5000 particles) are distributed over the stellar volume using the calculated profile. The initial position and velocity are chosen so that the star approaches the massive black hole in a parabolic orbit with a periastron radius R_p . For all simulations the starting point is a radial distance of $100R_g$, and the mass of the black hole is assumed to be $10^6 M_\odot$ (except for the calculations related to Fig. 9, in which $10^5 M_\odot$ black holes are also considered).

4.1. Solar-Type Stars

We first consider the evolution of a solar-type star with $R_* = R_\odot$ and $M_* = M_\odot$ in a parabolic orbit with penetration factors $\beta_p = (R_t/R_p) = 1, 5,$ or 10 around a Schwarzschild black hole with a mass of $10^6 M_\odot$. In Figure 2, the solid lines indicate the orbits of the center of mass of the stars calculated with the SPH code, and the dashed lines indicate the orbits of the point-particle stars obtained with the geodesic equation. We note that the two estimates are indistinguishable in the cases of $\beta_p = 1$ and 5 . Because of the relativistic precession effect, the orbits with $\beta_p = 5$ and 10 intersect with themselves. Especially for $\beta_p = 10$, the periastron radius $R_p \sim 2.4R_g$ is close to the critical value $2R_g$, below which the star enters the black hole. The orbit tightly winds around the black hole. A fraction of the kinetic energy is dissipated during the breakup of the star, $\Delta E \sim GM_*^2/R_*$, but the effective deceleration is small, $\Delta v/v_p \sim (GM_* R_t/c^2 R_* R_g) \sim 10^{-4}$, where $v_p \sim c(R_g/R_t)^{1/2}$ is the orbital velocity at the periastron. Therefore, the center of mass of the distribution (solid lines) follows the orbit of the corresponding point particle (dashed lines). In the deep-penetration case of $\beta_p = 10$, the star is strongly disrupted after passing through the periastron. Snapshots of the particle distribution from the SPH simulations are shown in Figure 3. When the debris is located close to the critical radius $2R_g$, the orbital evolution of each debris element is sensitive to its own

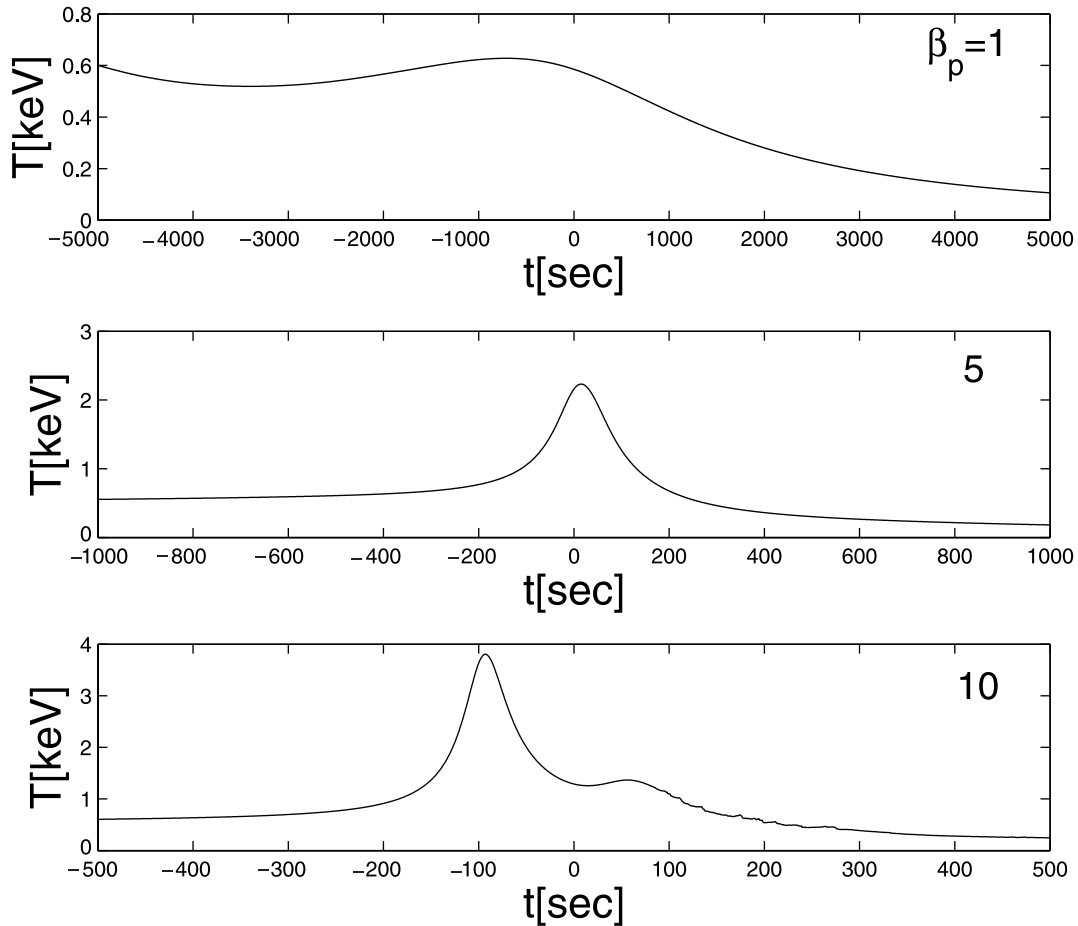


FIG. 4.—Average temperature for a solar-type star orbiting a Schwarzschild black hole. Time is relative to an origin at the instant of passage through the periastron of the orbit.

periastron. This causes the small difference between the SPH and point-particle estimates.

The evolution of the star's characteristic temperature T is plotted in Figure 4. This temperature is the value averaged over all particles. It provides a rough approximation to the thermal evolution of the star during the compressional heating and the subsequent reexpansion. The large optical depth of the star ensures that the photon diffusion time is much larger than any dynamical timescale; hence, the adiabatic compressional heating and cooling of the SPH simulation provide a reasonable approximation to the thermal evolution. The maximum temperatures for the values $\beta_p = 1, 5, 10$ are 0.69, 2.2, and 3.8 keV and are consistent with the rough estimate in equation (6). The average temperature T obtained from the SPH simulations, which in the unperturbed star is weighted toward the central regions, becomes characteristic also of the surface regions as shocks caused by the tidal compression reach the surface in a time comparable to the crossing time. This leads to photon fluences and luminosities compatible with the estimates (eqs. [7] and [8]). The SPH average temperature depends rather weakly on the penetration parameter, roughly as $T \sim \beta_p$, and the corresponding emission is concentrated in the X-ray band. The first compression point is attained before the periastron. When the trajectory of the center of mass intersects with itself within R_t , there are at least two compression points, in agreement with Luminet & Marck (1985). Therefore, the temperature has multiple peaks in the cases of $\beta_p \gtrsim 7$, including $\beta_p = 10$, as shown in Figure 4 (*bottom panel*).

The second compression is less significant, but the debris has a larger surface area. The emission at the second peak might have a fluence similar to that of the first one.

We evaluate the gravitational wave emission using the quadrupole formula. Although the velocity of the star at the periastron radius $v_p \sim c(R_g/R_p)^{1/2}$ is close to speed of light and the background geometry is not flat, the quadrupole formula provides an approximate estimate appropriate for our simple model. A more accurate treatment will be carried out in a future study. The waveforms of the gravitational waves emitted along the polar axis are shown in Figure 5. The thick and thin lines give two polarization components, h_+ and h_\times , respectively. The solid lines indicate the SPH estimates (the sum of the emission from all particles), while the dashed lines indicate the corresponding test-particle estimates. The source is assumed to be at a distance $D = 20$ Mpc. The trajectory in the case of $\beta_p = 1$ goes halfway around the black hole, within a radius comparable to the periastron radius (see Fig. 2), resulting in approximately a single cycle of gravitational wave emission. When the precession effect is larger ($\beta_p \gg 1$) a larger number of cycles are emitted, as one can see in Figure 5 ($\beta_p = 5$ and 10). Even in the case of $\beta_p = 10$, for which the star undergoes significant disruption (see the distributions at $t > 0$ in Fig. 3), the waveform based on the point-particle approximation agrees reasonably well with the SPH results.

We have also evaluated the evolution of a “dust” star with the same initial conditions, i.e., one in which only gravity (the self-gravity of the star and the background) is taken into

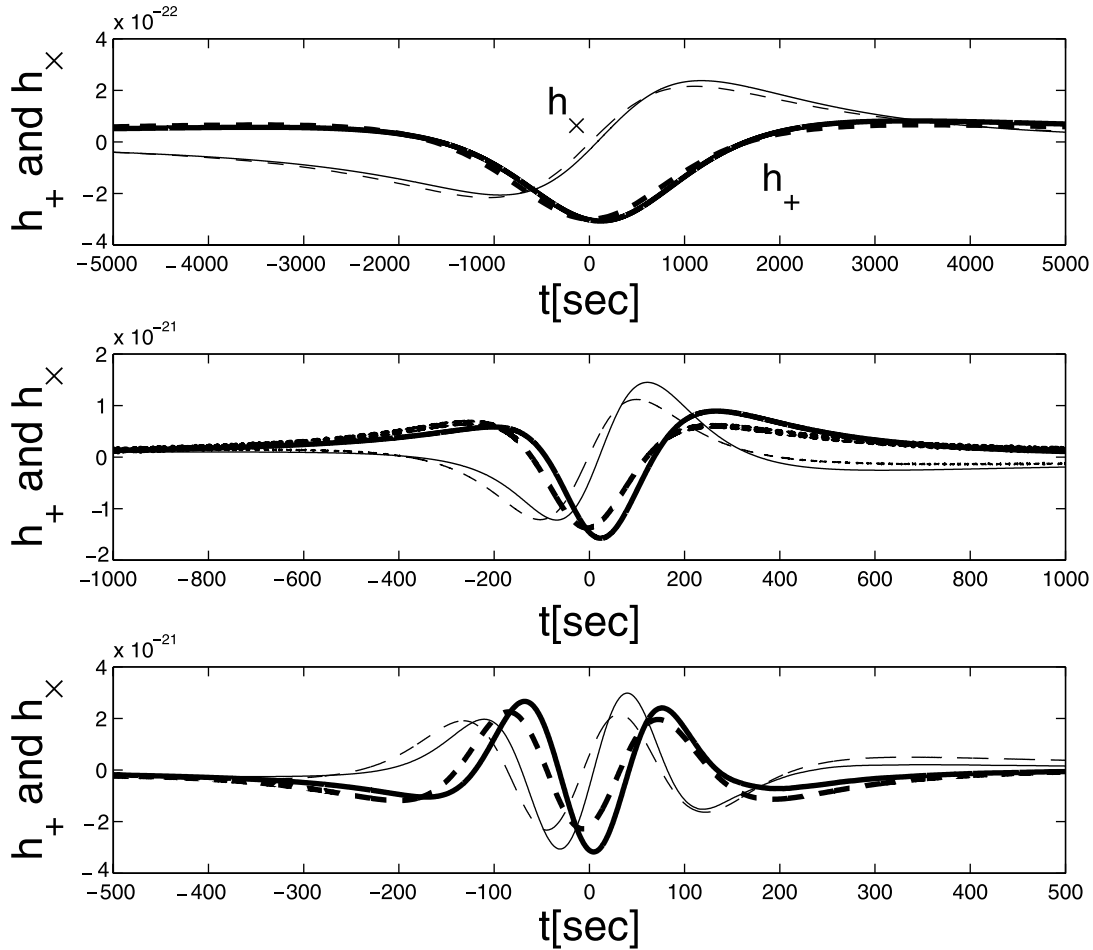


FIG. 5.—Gravitational waves from a solar-type star orbiting around a Schwarzschild black hole ($\beta_p = 1, 5$, or 10): SPH calculations (*solid lines*) and point-particle estimates (*dashed lines*), h_+ (*thick lines*) and h_\times (*thin lines*), and $M_h = 10^6 M_\odot$ and $D = 20$ Mpc.

account and the hydrodynamic module in the SPH code is turned off (zero pressure). The resulting gravitational wave emission is almost identical to that evaluated in the SPH calculation including hydrodynamics. This (and the agreement of the SPH and point-particle estimates) suggests that the gravitational wave signal during the disruption process is insensitive to the equation of state and to the detailed inner structure of the star. However, the detection of gravitational waves would provide information about the stellar orbit and the black hole.

In order to see the effect of the black hole spin on the star's temperature and gravitational wave emission, we have evaluated the evolution of a star orbiting around maximally rotating Kerr black holes. The orbits are assumed to be in the equatorial plane, and direct (prograde) and retrograde orbits are considered. The penetration factor is fixed at $\beta_p = 5$ for both cases. The top panel of Figure 6 shows the temperature of the star, while the middle and bottom panels show the two polarization components of the gravitational radiation along the polar axis. The temperature evolutions are similar, but the gravitational wave signal depends on the spin of the black hole. Thus, gravitational wave observations might allow a determination of, or constraints on, the black hole spin.

In our SPH code, the hydrodynamics is calculated in a Kerr black hole background written in the (ingoing) Kerr-Schild form, which are horizon-penetrating and suitable for tracking the evolution of stars orbiting closely around the horizon.

However, the Kerr-Schild time is in a rotating frame. The Boyer-Lindquist time, which is in a fixed frame, might be closer to what a distant observer sees. For comparison, we plot the wave signal results as functions of Boyer-Lindquist and Kerr-Schild times in Figure 7, in which a solar-type star is assumed to be orbiting around a black hole with penetration factor $\beta_p = 5$. The two waveforms are almost identical for the Schwarzschild black hole case (Fig. 7, *middle panel*), but for Kerr cases the difference could be noticeable (the difference of the strains at the same time is a few 10% level).

4.2. He Stars

The passage of giant stars within $\sim 10^2$ – $10^4 R_g$ from a black hole of mass $\sim 10^6 M_\odot$, as well as tidal encounters between such stars in the nuclear region, can lead to the loss of the low-density stellar envelope. The tidal stripping leaves the dense core (usually an He star) as its end product. Within a few hundred R_g from such a massive black hole, the stellar population is likely to consist overwhelmingly of compact stars including He stars. The rate of capture and tidal disruption of He stars by the massive black hole is expected to be higher than that of solar-type stars.

We have studied the evolution of He stars of mass $M_* = 0.5 M_\odot$ and radius $R_* = 0.08 R_\odot$ orbiting a Schwarzschild black hole of $10^6 M_\odot$. The ratio of R_t to the horizon scale R_g is $R_t/R_g \sim 2.4(R_*/0.08 R_\odot)(M_*/0.5 M_\odot)^{-1/3} (M_h/10^6 M_\odot)^{-2/3}$. Since the critical periastron radius $\sim 2R_g$, within which a star is

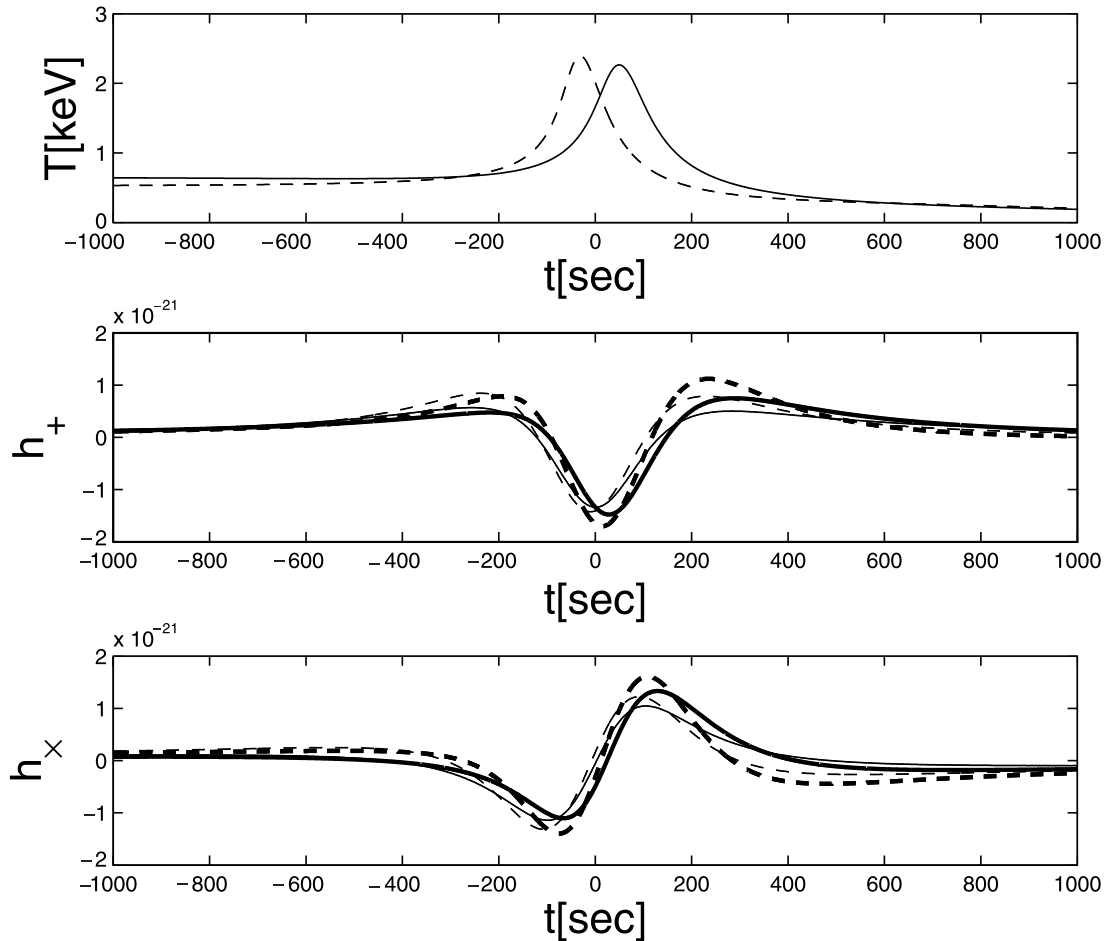


FIG. 6.—Average temperature and gravitational radiation for solar-type stars around a maximally rotating Kerr black hole in a $\beta_p = 5$ orbit. (a) Temperature (solid line, prograde; dashed line, retrograde). (b) h_+ : SPH estimates (thick line) and point-particle estimates (thin line). (c) h_x . Parameters are $M_h = 10^6 M_\odot$, $D = 20$ Mpc.

captured by the black hole, is close to the tidal radius R_t , the tidal heating of He stars in parabolic plunge orbits is relatively less severe than for solar-type stars, since only modest values of β_p values are possible, for this hole $M_h = 10^6 M_\odot$. However, an He star is more compact and in the unperturbed state has a larger central (and average) temperature than a solar star to begin with. In this case, numerical results for $\beta_p = 1$ show that the tidal compression effect leads to larger average temperatures (Fig. 8) than for the corresponding orbits in solar-type stars. The shock-heated surface reaches temperatures of several keV. Thus, while the radius squared is down by ~ 160 , the fourth power of the temperature is up by ~ 300 and the X-ray flare has a peak luminosity comparable to equation (8), but with a harder spectrum.

Since the relativistic precession effect is large, the stellar orbit winds tightly around the black hole, and multiple cycles of gravitational waves are emitted. The gravitational wave strain is, for the same β_p , about 1 order of magnitude larger than for the corresponding solar-type stars, since the periastron is closer in. In this case also, the point-particle approximation describes the SPH results reasonably well.

5. OBSERVATIONAL PROSPECTS

The tidal disruption rate depends on the mass of the black hole, the stellar density, velocities in the galactic nucleus, and the rate at which radial loss cone orbits are depleted. The

tidal disruption rate of solar-type stars in samples of nearby galaxies was estimated as $10^6 - 10^4 \text{ yr}^{-1}$ (Syer & Ulmer 1999; Magorrian & Tremaine 1999). The highest disruption rates (one star per 10^4 yr) occur in faint ($L \lesssim 10^{10} L_\odot$) galaxies. The corresponding disruption rates for He stars are likely to be higher than these values. Flares occur much less frequently in larger galaxies, partly because such galaxies have black holes with $M_h \gtrsim 10^8 M_\odot$ that swallow main-sequence stars whole, and partly because such galaxies are less centrally concentrated, meaning that their timescales are much longer.

Observational constraints on disruption rates are uncertain. A tidal disruption event, besides the prompt X-ray flash discussed here, is expected also to produce a long-duration luminous photon flare in the fallback phase (weeks to months after the stellar disruption), which may be looked for in all-sky soft X-ray surveys. Komossa (2001) argued that the convincing detection of such a tidal disruption event would be the observation of an event that fulfills the following three criteria: (1) the event should be of finite duration (a “flare”); (2) it should be very luminous, up to $\sim 10^{45} \text{ ergs s}^{-1}$ at maximum; and (3) it should reside in a galaxy that is otherwise perfectly nonactive. The *ROSAT* All-Sky Survey (RASS) detected several candidates that fulfill the criteria (summarized in Komossa 2001). Recent *Chandra* observations show that for three of the candidates the X-ray flux decline is consistent

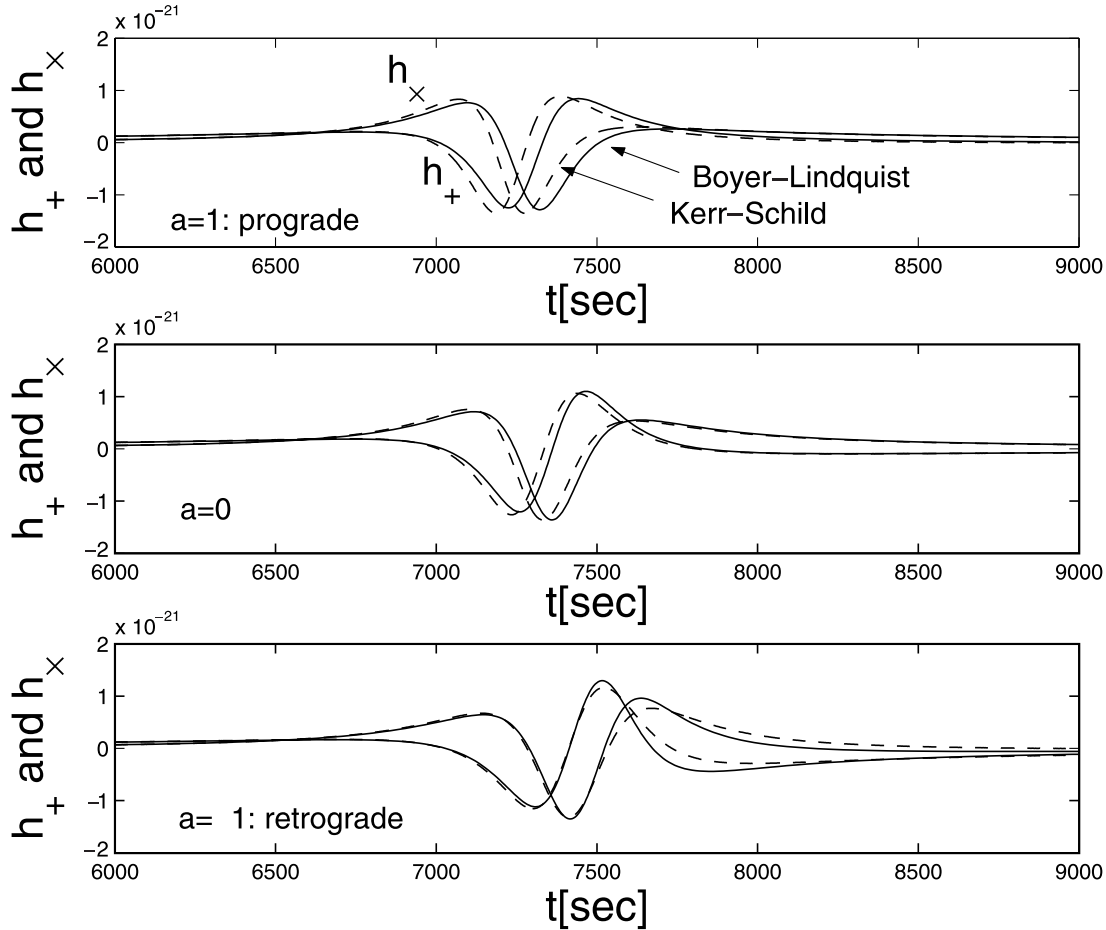


FIG. 7.—Point-particle estimates on gravitational waveforms h_+ and h_\times in Boyer-Lindquist coordinates (solid lines) and Kerr-Schild coordinates (dashed lines). Solar-type stars around a $10^6 M_\odot$ black hole in a $\beta_p = 5$ orbit. (a) Maximally rotating Kerr black hole (prograde). (b) Schwarzschild black hole. (c) Maximally rotating Kerr black hole (retrograde) $D = 20$ Mpc.

with the $t^{-5/3}$ decay predicted for the fallback phase (Halpern et al. 2004). From the statistics of RASS, Donley et al. (2002) obtained a rate of $\sim 10^{-5} \text{ yr}^{-1}$, which is consistent with the theoretical predictions.

As we have shown in § 5, a gravitational wave burst with a large amplitude is expected to be associated with a prompt X-ray flash when a solar-type or He star passes near the horizon of a massive black hole with mass of $10^6 M_\odot$. This gravitational signal might be detectable by *LISA* up to $D \sim 20$ Mpc. The Virgo Cluster consists of ~ 2000 galaxies, so one might detect such a gravitational wave burst once per 10–1000 yr.⁵ The flux of the prompt X-ray flash from a source in Virgo is about $\sim 10^{-10} \text{ ergs cm}^{-2} \text{ s}^{-1}$, which for a typical duration of 10 s, which is detectable with the $23' \times 23'$ FOV *Swift* XRT detector but falls 1 order of magnitude below the sensitivity of the *Swift*

⁵ High values of the penetration factor β_p are only possible for relatively low mass supermassive black holes $M_h \lesssim 10^7 M_\odot$. Recent surveys of supermassive black hole candidates give somewhat larger mass estimates (a few $10^7 M_\odot$; e.g., Kormendy & Gebhardt 2001). If massive black holes in the Virgo Cluster would predominantly have such larger masses, the event rates of gravitational wave bursts associated with strong X-ray flashes could be lower than we calculated here. On the other hand, the dynamical black hole mass estimates in our own Milky Way nucleus (Genzel et al. 2003; Ghez et al. 2003) indicate that many, if not most, modest-sized galaxies may have black holes in the mass range $\sim 10^6 M_\odot$, and these may constitute the majority of galaxies.

BAT detector, whose 2 sr field of view and rapid slewing response would be key advantages. This flux is well above the sensitivity limits of the *Chandra* and *XMM-Newton* X-ray satellites, but their fields of view are narrow and slewing takes hours, so the chances are better for detecting the longer (days to weeks) duration fallback X-ray flare, which with the same spacecraft is detectable out to at least 200 Mpc. The prompt X-ray flare, on the other hand, whose duration is of order ~ 10 s at a peak luminosity of $\sim 10^{42} \text{ ergs s}^{-1}$, may require a future wide field of view detector, a factor of 30 more sensitive than the BAT on board *Swift*. The predicted time decay $\propto t^{-1/2}$ behavior would help to distinguish these flares from type I X-ray bursts. The detection would allow us to observe the moment of the tidal disruption and help confirm the detection of simultaneous gravitational waves.

The detection of the prompt X-ray emission could provide a constraint on the mass of the massive black hole involved in the tidal disruption process. When a star passes near a massive black hole, the smallest distance to which the star in a parabolic or hyperbolic orbit can approach and yet not be captured by the black hole is $\sim 2R_g$ (Schwarzschild black hole). The ratio between this radius and the tidal radius R_t gives the maximum value of the penetration factor β_p ($\beta_p \lesssim 12$ and 56 for 10^6 and $10^5 M_\odot$ black hole, respectively). The characteristic temperature of a solar-type star before the close passage is sub-keV. Our numerical results show that the tidal

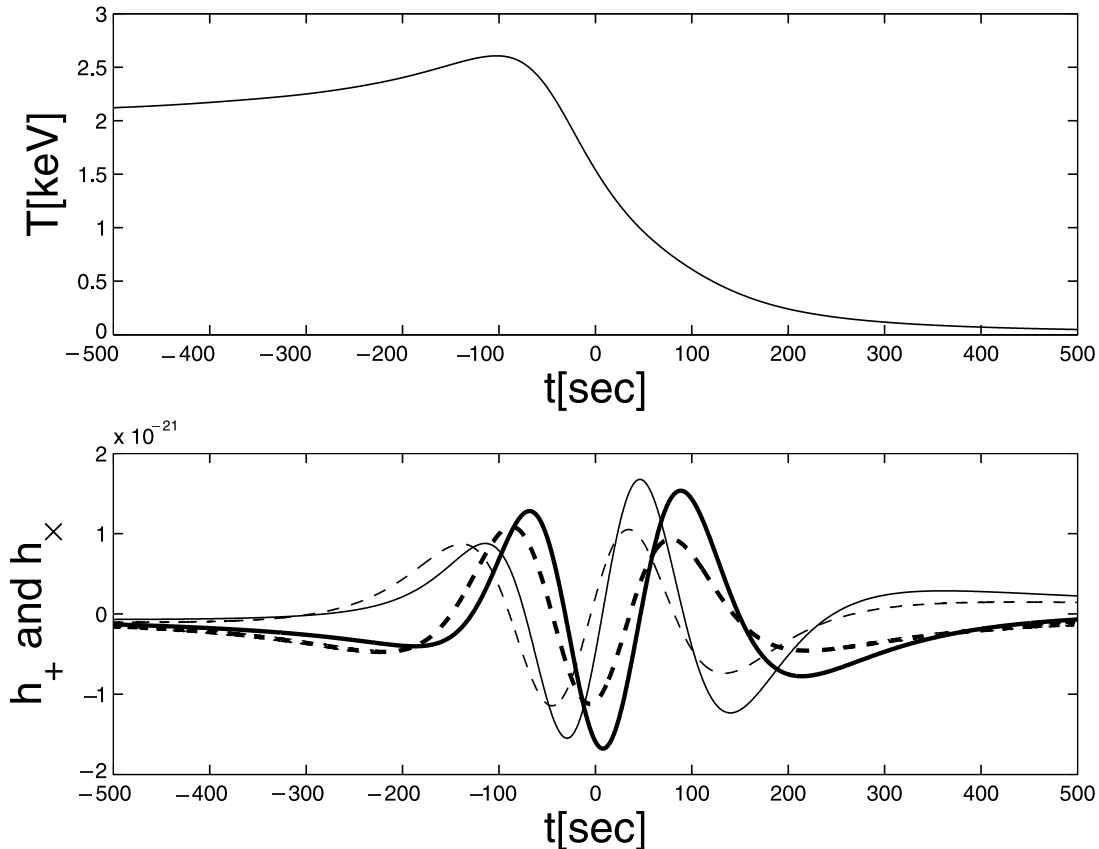


FIG. 8.—Average temperature and gravitational radiation from an He star in a $\beta_p = 1$ orbit around a Schwarzschild black hole of $10^6 M_{\odot}$. (a) Temperature. (b) Gravitational wave strain: h_+ (thick line) and h_{\times} (thin line), SPH estimates (solid line), and point-particle estimates (dashed line). Parameters are $D = 20$ Mpc, $M_s = 0.5 M_{\odot}$, and $R_* = 0.08 R_{\odot}$.

compression can increase this temperature by a factor of $\sim \beta_p$. In Figure 9, we plot the maximum temperature at the moment of the tidal compression as a function of the penetration factor β_p . The crosses and circles indicate the results for 10^6 and $10^5 M_{\odot}$ black holes, respectively. In the case of the $10^6 M_{\odot}$

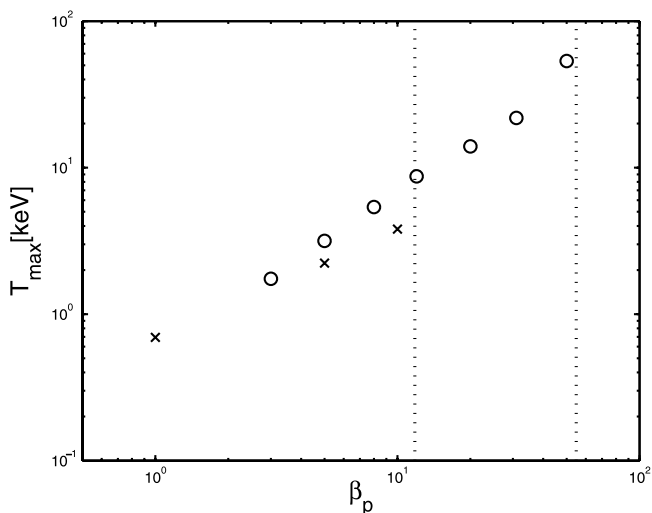


FIG. 9.—Average temperature at the moment of maximum tidal compression vs. penetration factor β_p : a solar-type star orbiting around a Schwarzschild black hole of $10^5 M_{\odot}$ (circles) or $10^6 M_{\odot}$ (crosses). The vertical lines indicate the maximally allowed value of the penetration factor $\beta_{p, \max}$. For a solar-type star, $\beta_{p, \max} \sim 12$ ($10^6 M_{\odot}$ black hole) and ~ 56 ($10^5 M_{\odot}$ black hole).

black hole, the temperature is about several keV at most. If an X-ray flare with much high temperature is detected in a future mission, it might indicate that the black hole involved in the tidal disruption process has a mass much smaller than $10^6 M_{\odot}$ or that an intermediate-mass black hole might be harbored in the galaxy.

6. CONCLUSIONS

We have numerically investigated the evolution of solar-type and He-type stars that are captured and disrupted by massive black holes with mass of 10^5 – $10^6 M_{\odot}$. We have shown that for both types of stars, plunge orbits that approach the horizon produce gravitational wave bursts with large amplitudes, which may be detectable by *LISA* up to $D \sim 20$ Mpc. Even though the stars undergo significant disruption, the waveforms of the gravitational signal can be reasonably well approximated by a point-particle approximation. We have also shown that the gravitational wave signal during the disruption process is largely insensitive to the equation of state and to the detailed inner structure of the star. For the same penetration parameter β_p (ratio of tidal to periastron radius), the waveforms of main-sequence and He stars differ considerably in shape, although deep-penetration (e.g., $\beta_p = 10$) main-sequence waveforms have some resemblance to critical penetration ($\beta_p = 1$) He star waveforms. For large Kerr rotation parameters, the waveform shape and polarization is sensitive to the black hole rotation and its sign. In addition to long-term (days to years) X-ray flares, we also predict a prompt X-ray flash, of luminosity $L_X \sim 10^{42}$ ergs s^{-1} and duration ~ 10 s

associated with the gravitational wave bursts. The characteristic spectral temperature can give constraints on the black hole mass.

We thank M. Rees, S. Sigurdsson, T. Alexander, S. Mahadevan, and the referee for valuable comments. This work

is supported by NASA NAG5-13286, NASA NAG5-10707, NSF AST 00-98416, the Monell Foundation, the Merle Kingsley fund, and the Pennsylvania State University Center for Gravitational Wave Physics, funded under cooperative agreement by NSF PHY 01-14375.

APPENDIX

TIDAL COMPRESSION AND SHOCKS: NUMERICAL STUDY

When a star penetrates within the tidal radius R_t of a massive black hole, the tidal acceleration begins to be dominant compared to self-gravity. The star departs from hydrostatic equilibrium, and it undergoes a significant compression. The compression eventually should be halted and reversed by the buildup of pressure in a highly flattened pancake configuration (Carter & Luminet 1982). For deep-encounter cases (penetration factors $\beta_p \gg 1$), we expect that a shock occurs at the end of the strong compression phase.

We investigate the shock formation process by means of a relativistic Lagrangian code based on the Godunov method with an exact Riemann solver (Kobayashi et al. 1999). Since the compression is governed by the tidal force perpendicular to the orbital plane, we study a non-self-gravitating gas slab in a varying gravitational potential. The effects of the tidal force can be simulated through

$$\frac{d^2r}{dt^2} = -\frac{GM_h}{R^3}r, \quad (\text{A1})$$

$$R = \frac{2R_p}{1 + \cos\theta}, \quad (\text{A2})$$

$$\frac{d\theta}{dt} = \left(\frac{GM_h}{8R_p^3}\right)^{1/2} (1 + \cos\theta)^2, \quad (\text{A3})$$

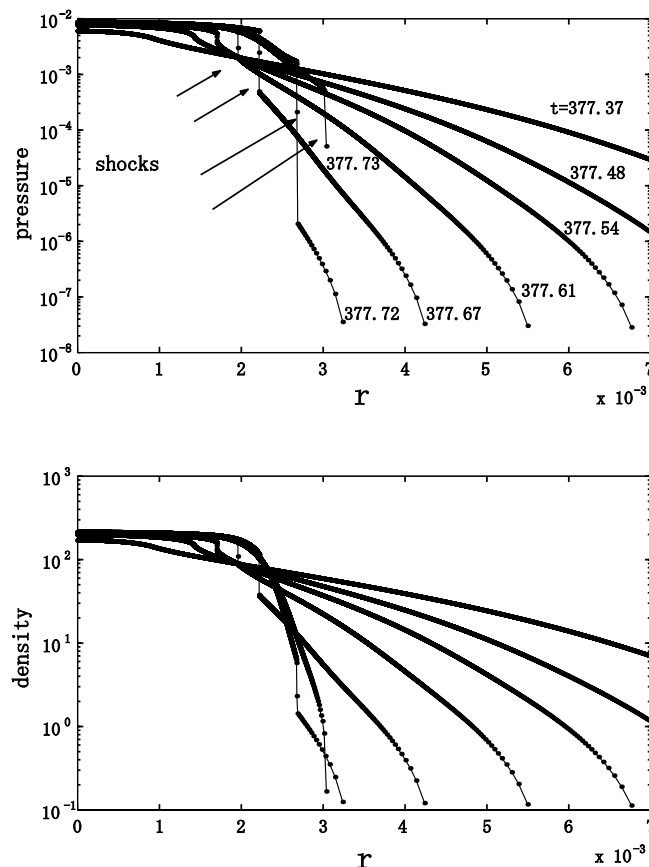


FIG. 10.—Shock formation: Time evolution of the pressure and density in the tidal compression stage. The r -coordinate is the distance from the orbital plane in units of the initial stellar radius R_* . Time is in units of R_*/c , with $t = 0$ set at the instant when the star is at $R = R_t$. The density is normalized to an initial central density of unity, and the initial central polytropic pressure (for $c = 1$) is $\sim 1.14 \times 10^{-6}$.

where r is the distance from the orbital plane and $R(t)$ is the distance to the black hole for a Newtonian parabolic orbit. The hydrodynamic code without the tidal force term has been tested in problems involving ultrarelativistic flows, strong shocks, and discontinuities (Kobayashi et al. 1999). In order to test the tidal effects in the code, we numerically evolved a gas blob in a very rare and low pressure medium. For an initial position r_0 and velocity $\dot{r}_0 = 0$ and a constant tidal field $R = \text{constant}$, the numerically obtained position of the blob is well described by the analytic solution $r(t) = r_0 \cos kt$, where $k = (GM_h/R^3)^{1/2}$, except for the last moment $r \sim 0$ when the buildup of pressure at the center decelerates the blob.

In the following calculations, we consider a stellar encounter characterized by $\beta_p = R_t/R_p = 10$ and $R_t/R_g \sim 24$. The latter corresponds to a solar-type star and a $10^6 M_\odot$ black hole. We assume a polytropic distribution with an adiabatic index $\Gamma = 5/3$ as the initial density and pressure distributions at $R(0) = R_t$. The central density is $\rho_c \simeq 5.9907\bar{\rho} \simeq (9M_*/2\pi R_*^3)$. We express the density ρ in units of this central density ρ_c and the pressure in units of $\rho_c c^2$. The polytropic values become zero at the stellar surface $r = R_*$. For numerical reasons, we evaluate the evolution of the fluid elements within the radius $R'_* (< R_*)$ within which 99% of the star mass is contained in the planar geometry model ($R'_* \sim 0.815R_*$). The pressure and density at $r = R'_*$ are initially smaller than the central values by factors of ~ 90 and ~ 15 , respectively. We consider a uniform ambient external medium. The pressure is assumed to be continuous at $r = R'_*$ and constant outside, while the outside density is 10^{-5} of the initial central density. All fluid elements in the star and ambient are initially at rest in the star's comoving frame. A reflection boundary condition is imposed at the center $r = 0$.

Figure 10 shows the results for a 3000 zone mesh with equal initial widths. In the figure we have plotted only the stellar region covered by 2400 zones. After the star passes through the periastron at $t \sim 368.42R_*/c$, the central pressure and density sharply increase. At $t = 377.37R_*/c$, they are larger than the initial value by a factor of ~ 5200 and ~ 170 , respectively. At this point, a shock starts to propagate from the center and heats up the outer layers (see Fig. 10). We performed an additional simulation in which the initial pressure and density are assumed to be uniform throughout the star and equal to the central values of the polytropic distributions. This second calculation also shows a shock developing right after the periastron passage, which heats up the stellar material. This result indicates that the shock formation is rather insensitive to the choice of the stellar density distribution.

REFERENCES

- Ayal, S., Livio, M., & Piran, T. 2000, *ApJ*, 545, 772
 Bender, P., et al. 1998, *LISA: Laser Interferometer Space Antenna*, for the Detection and Observation of Gravitational Waves: Pre-Phase A Report (MPQ Rep. 233; Garching: MPI)
 Campanelli, M., Khanna, G., Laguna, P., Pullin, J., & Ryan, M. P. 2001, *Classical Quantum Gravity*, 18, 1543
 Carter, B., & Luminet, J. P. 1982, *Nature*, 296, 211
 ———. 1983, *A&A*, 121, 97
 Donley, J. L., Brandt, W. N., Eracleous, M., & Boller, Th. 2002, *AJ*, 124, 1308
 Evans, C. R., & Kochanek, C. S. 1989, *ApJ*, 346, L13
 Finn, L. S., Mohanty, S. D., & Romano, J. D. 1999, *Phys. Rev. D*, 60, 601101
 Freitag, M. 2003, *ApJ*, 583, L21
 Genzel, R., et al. 2003, *Nature*, 425, 934
 Ghez, A. M., Salim, S., Hornstein, S. D., Tanner, A., Morris, M., Becklin, E. E., & Duchene, G. 2003, *ApJ*, submitted (astro-ph/0306130)
 Halpern, J. P., Gezari, S., & Komossa, S. 2004, *ApJ*, 604, 572
 Hils, D., & Bender, P. L. 1995, *ApJ*, 445, L7
 Hughes, S. A. 2002, *MNRAS*, 331, 805
 Ivanov, P. B. 2002, *MNRAS*, 336, 373
 Ivanov, P. B., & Novikov, I. D. 2001, *ApJ*, 549, 467
 Khokhlov, A., Novikov, I. D., & Pethick, C. J. 1993, *ApJ*, 418, 181
 Kobayashi, S., Piran, T., & Sari, R. 1999, *ApJ*, 513, 669
 Komossa, S. 2001, in *Lighthouses of the Universe*, ed. M. Gilfanov & R. Sunyaev (Heidelberg: Springer), 436
 Kormendy, J., & Gebhardt, K. 2001, in *AIP Conf. Proc.* 586, 20th Texas Symp. on Relativistic Astrophysics, ed. J. C. Wheeler & H. Martel (Melville: AIP), 363
 Lacy, J. H., Townes, C. H., & Hollenbach, D. J. 1982, *ApJ*, 262, 120
 Laguna, P., Miller, W. A., & Zurek, W. H. 1993a, *ApJ*, 404, 678
 Laguna, P., Miller, W. A., Zurek, W. H., & Davies, M. B. 1993b, *ApJ*, 410, L83
 Landau, L. D., & Lifshitz, E. M. 1975, *The Classical Theory of Fields* (New York: Pergamon)
 Li, L. X., Narayan, R., & Menou, K. 2002, *ApJ*, 576, 753
 Loeb, A., & Ulmer, A. 1997, *ApJ*, 489, 573
 Luminet, J. P., & Marck, J. A. 1985, *MNRAS*, 212, 57
 Magorrian, J., & Tremaine, S. 1999, *MNRAS*, 309, 447
 Marck, J. A., Lioure, A., & Bonazzola, S. 1996, *A&A*, 306, 666
 Nolthenius, R. A., & Katz, J. I. 1982, *ApJ*, 263, 377
 Phinney, E. S. 1989, in *IAU Symp.* 136, *The Center of the Galaxy*, ed. M. Morris (Dordrecht: Kluwer), 543
 Rees, M. 1988, *Nature*, 333, 523
 Sigurdsson, S., & Rees, M. J. 1997, *MNRAS*, 284, 318
 Syer, D., & Ulmer, A. 1999, *MNRAS*, 306, 35
 Ulmer, A. 1999, *ApJ*, 514, 180
 Ulmer, A., Paczynski, B., & Goodman, J. 1998, *A&A*, 333, 379